GeV electron beams from cm-scale channel guided laser wakefield accelerator*

K. Nakamura,† B. Nagler,‡ Cs. Tóth, C. G. R. Geddes,
C. B. Schroeder, E. Esarey, and W. P. Leemans§
Lawrence Berkeley National Laboratory,
University of California, Berkeley, CA 94720, USA

A. J. Gonsalves¶ and S. M. Hooker
University of Oxford, Clarendon Laboratory, Oxford, UK

(Dated: February 20, 2007)

Abstract

Laser-wakefield accelerators (LWFA) can produce electric fields of order 10-100 GV/m suitable for acceleration of electrons to relativistic energies. The wakefields are excited by a relativistically intense laser pulse propagating through a plasma and have a phase velocity determined by the group velocity of the light pulse. Two important effects that can limit the acceleration distance and hence the net energy gain obtained by an electron are diffraction of the drive laser pulse and particle-wake dephasing. Diffraction of a focused ultra-short laser pulse can be overcome by using preformed plasma channels. The dephasing limit can be increased by operating at a lower plasma density, since this results in an increase in the laser group velocity. Here we present detailed results on the generation of GeV-class electron beams using an intense femtosecond laser beam and a 3.3 cm long preformed discharge-based plasma channel [W.P. Leemans *et al.*, Nature Physics **2**, 696-699 (2006)]. The use of a discharge-based waveguide permitted operation at an order of magnitude lower density and 15 times longer distance than in previous experiments that relied on laser preformed plasma channels. Laser pulses with peak power ranging from 10-50 TW were guided over more than 20 Rayleigh ranges and high-quality electron beams with energy up to 1 GeV were obtained by channelling a 40 TW peak power laser pulse. The dependence of the electron beam characteristics on capillary properties, plasma density, and laser parameters are discussed.

PACS numbers: 41.75.Ht, 41.75.Jv, 52.38.Kd

I. INTRODUCTION

Over the past decade acceleration gradients in the 10's to 100's GV/m have been generated in laser wakefield accelerator (LWFA) experiments,[1–7] which is three orders of magnitude higher than in conventional linacs. Although it is straightforward to achieve such a high acceleration gradients in laser wakefield accelerators[8,9], the electron beams (e-beams) from such accelerators had 100% energy spread until 2004, when the production and measurements of high quality (i.e., low energy spread) was reported[10–12]. To obtain the monoenergetic bunches, two groups used relatively large laser spot sizes[10,12]. This effectively increases the diffraction (or Rayleigh) range, Z_R of the laser beam, permitting propagation over distances on the order of the gas jet length. For example, experiments performed at Rutherford Appleton Laboratory (RAL) by Mangles *et al.* employed a 16 TW, 40 fs laser pulse focused (25 μm spot size, 2.5×10^{18} W/cm^2) on the plume of a gas jet with a plasma density of 2×10^{19} cm^{-3}. A narrow energy spread bunch was observed at 78 ± 2 MeV with 20 pC of charge[10]. Experiments performed at Laboratoire d'Optique Appliquée (LOA) by Faure *et al.* used a 30 TW, 33 fs laser pulse focused [21 μm spot size in full-width at half-maximum (FWHM) 3.2×10^{18} W/cm^2] on the plume of a gas jet with a plasma density of 6×10^{18} cm^{-3}. A narrow energy spread bunch was observed at 170 ± 20 MeV with 500$\pm$200 pC of charge[12].

The Lawrence Berkeley National Laboratory (LBNL) experiments[11] used a 9 TW, 55 fs laser pulse focused to a relatively tight spot size (8.5 μm FWHM). To mitigate the short Z_R of the beam, a 2 mm long laser produced preformed plasma channel was used to guide the laser beam through the gas jet. The driving laser beam generated 85 MeV e-beams containing 0.3 nC bunch charge, with only 9 TW of laser peak power[11,13,14].

The importance of the accelerator length, and how to extend it, has been discussed extensively. As an example, during the 1995 Kardamyli Workshop on second generation plasma-based accelerators, design studies for a 1 GeV LWFA were carried out in the laser guiding and acceleration working group[15]. The main conclusion of the study was that extending the propagation of a laser pulse beyond Z_R, up to the dephasing distance, was an essential element of a future LWFA. Much higher net energy gains can be realized for the same amount of input laser power by extending the acceleration distance beyond Z_R. Guiding concepts relying on the use of preformed plasma channels have been pursued by

several groups around the world[14,16–23].

The plasma channels in the LBNL experiments[11] were produced using the ignitor-heater concept[17] and were shown to guide laser pulses with relativistic intensities ($> 10^{18}$ W/cm^2)[11] that are relevant for particle acceleration over many Z_R. The method relied on rapidly heating a laser-ionized filament using inverse Bremsstrahlung heating with a 200-300 ps, 0.1 J level laser pulse. Since the heating efficiency scales with the square of the plasma density, high plasma densities are required ($\geq 10^{19}$ cm^{-3}). This limits the group velocity of the laser pulse and the phase velocity of the plasma wake and hence the maximum achievable electron beam energy.

The dephasing length over which electrons outrun the wake and slip into the decelerating phase is determined by the group velocity of the laser, and limits the distance over which acceleration occurs. The linear dephasing length is given by $L_{\rm deph} = \lambda_p^3/\lambda^2 \propto n_p^{-3/2}$, where λ_p is the plasma wavelength, λ the laser wavelength, and n_p the plasma density. The linear depletion length over which the laser loses energy to the plasma wave also scales as $L_{\rm dep} \sim a_0^{-2}\lambda_p^3/\lambda^2 \propto n_p^{-3/2}$, and for laser intensities such that $a_0 \sim 1$, these length scales are approximately equal. For relativistic laser intensities $a_0 \sim 1$, the accelerating electric field of the plasma wave is on the order of $E_0 = mc\omega_p/e \propto n_p^{1/2}$. Therefore the energy gain over a dephasing (or depletion) length scales as $W \propto 1/n_p$. This scaling law indicates that to achieve higher energy particle beams requires lower density plasmas (and longer plasma channels), which motivates the use of capillary discharge waveguides in the present work.

To circumvent the density limitation imposed by the ignitor-heather method and allow the production of multi-cm scale plasma channels, we have employed a gas-filled capillary discharge waveguide[20,24] to guide relativistically intense laser pulses in cm-scale, lower density plasma channels. In this paper we discuss the recently reported generation of GeV electron beams using these hydrogen filled capillary discharge-based plasma channels[25].

II. EXPERIMENTAL SET-UP

The experiments used the short pulse, high peak power and high repetition rate Ti:Al_2O_3 laser system[26] of the LOASIS facility at LBNL. Low energy laser pulses (of wavelength $\lambda \simeq 0.8$ μm) from a Ti:Al_2O_3 laser oscillator were first temporally stretched, amplified to approximately 3.5 J/pulse, and then compressed using a grating based optical compressor.

Following compression, the laser beam was focused by an f/25 off-axis paraboloid of 200 cm focal length to a spot size $w = 25$ μm at the entrance of a capillary discharge waveguide. The lay-out of the experiment in shown in Fig. 1. The peak power P of the laser was varied by adjusting both the pulse duration and laser energy. At full energy and optimum compression (37 fs FWHM duration), $P \simeq 40$ TW, resulting in a calculated peak intensity $I = 2P/\pi r_s^2 \simeq 4 \times 10^{18}$ W/cm^2 and a normalized vector potential $a_0 \simeq 8.6 \times 10^{-10} \lambda[\mu\text{m}] I^{1/2}[\text{W/cm}^2] \simeq 1.4$.

The capillaries were laser machined into 33 mm long sapphire blocks with diameters ranging from 190 μm to 310 μm. Hydrogen gas, introduced through holes near the capillary ends, was ionized by striking a discharge between electrodes located at each end of the capillary. Measurements[20] and modelling[27,28] showed that a fully ionized, approximately parabolic channel is formed. This is also confirmed by the absence of significant ionization induced blueshifting of the laser spectrum when proper guiding conditions are achieved. Previous experiments[24] demonstrated channeling of non-relativistically intense laser pulses with $I \lesssim 10^{17}$ W/cm^2 in 30–50 mm long capillaries, which did not generate electron beams.

The electron magnetic spectrometer utilized a round pole magnet, with an effective radius of 19.5 cm and a peak field strength of 1.2 T. The magnet deflected the electrons vertically downward onto two phosphor screens mounted on the exit flanges of the vacuum chamber. Four synchronously triggered 12-bit charge-coupled device (CCD) cameras imaged a 75 cm long (bottom) and a 45 cm long (forward) phosphor screen, allowing simultaneous single shot measurement of electrons from 0.03 GeV to 0.15 GeV (bottom) and 0.17 GeV to 1.1 GeV (forward). The electron beam divergence and energy spread were calculated from the spectral data assuming an axisymmetric electron beam profile (i.e., equal horizontal and vertical divergence), and by using the imaging properties of the magnetic spectrometer which were calculated using a second order electron transport model[29] and the measured magnetic field map. The electron beam divergence was determined from the e-beam size in the horizontal plane, taking into account the transverse defocusing properties of the magnet. Under the assumption of an axisymmetric beam, the intrinsic resolution of the spectrometer at a specific monoenergetic energy, δE_{mono}, can then be calculated for a given beam divergence. The real energy spread of an electron beam δE_{beam} is then calculated by deconvolving the effect of finite divergence from the measured e-beam profile δE_{img} using $\delta E_{img} = \sqrt{\delta E_{beam}^2 + \delta E_{mono}^2}$.

Due to the finite angular acceptance of the system, the spectrometer has an intrinsic error

bar in the determination of the absolute energy value. Shown in Fig. 2 is the calculated screen position as a function of the incident electron energy for electrons propagating along the axis (0 degree) or at angles of ± 0.25 and ± 0.5 degrees in the vertical plane. For example, one can see that if a 0.94 GeV electron beam enters the spectrometer with an incident angle of 0.25 degree, it would be measured as a 1.0 GeV beam. To evaluate the error bar, the angular fluctuation of the beam was statistically analyzed from the position of the beam in the horizontal plane and found to be 0.21 degree in rms. With assumption of symmetric behavior in both planes, the error bars on 1.0 and 0.5 GeV are shown in Fig. 2, and are (+0.058, -0.052), and (+0.026, -0.024), respectively. The bunch charge was obtained from the intensity on the phosphor screen, that was cross-calibrated against an integrating current transformer.

III. GUIDING AND ELECTRON BEAM GENERATION

The relativistic electron beam generation via capillary discharge guided laser wakefield acceleration was experimentally studied by making use of 33 mm long capillaries with diameters of 190, 225, and 310 μm. The results were analyzed against the delay between the onset of the discharge current and the arrival of the laser beam, plasma density, laser energy, and laser intensity. In the following, the term density means the estimated axial electron density from the measured Hydrogen gas pressure inside of the capillary using the scaling law in Ref. 30. The parameters of the generated electron beams were found to be sensitive and exhibited a complicated interdependence on all these parameters. Timing jitter between discharge and laser arrival, pointing fluctuations, and laser power fluctuations were significant for this first generation of experiments. By taking advantage of the high repetition rate experimental system, data sets containing several thousands shots were taken for each capillary and analysis software was developed to find and sort shots with similar parameters, allowing a statistical evaluation of the overall performance.

Guiding was optimized by adjusting the initial gas density and the delay between onset of the discharge current and arrival of the laser pulse (see Fig. 3a). The measured discharge current was reproducible within shot-to-shot fluctuations of a few %, and had periodic ripples on its profile as shown in Fig. 3a. The laser beam transmission correlated with discharge current (Fig. 3a) and, for low power (<5 TW), transmission was above 90% for densities

ranging from 1.0 to 4.0 $\times$ 10^{18} cm^{-3} in a $\sim$100 ns timing window. Note that the jitter between the arrival time of a laser and the discharge current is not an intrinsic problem of the waveguide, because the $\sim$100 ns timing window is far larger than the jitter in the system which is a few ns. Figures 3b and 3c show laser beam profiles at the waveguide entrance and exit for 40 TW laser pulses with an input intensity $\sim 10^{18}$ W/cm^2 and a plasma density of $\simeq 2.7 \times 10^{18}$ cm^{-3}. This intensity is sufficiently high for large amplitude wake generation, self-trapping, and high-gradient electron acceleration as observed in the experiment (see below). The guiding performance was highly sensitive to input beam alignment with 15 μm displacement away from the optimum location (based on quality of guided beam) resulting in transmission drops on the order of 20%. Note that without a preformed plasma channel (laser injected ahead of discharge) transmission was below 5% and bulk damage was sustained to the capillary channel walls, indicating that self-ionization and relativistic self-focusing could not be relied on for guiding, as expected from short pulse propagation theory[31].

The threshold laser intensity for self-electron injection into a plasma wakefield was explored by changing laser pulse duration via the tuning of the inter-grating distance in the optical compressor, and laser energy via adjustment of the 532 nm Nd:YAG pumping power of the main amplifier system. Focal position changes when adjusting the level of pumping power on the cryogenically cooled amplifier crystal were found to be negligible ($< 0.1\ Z_R$) and no spot size changes were observed.

To evaluate the dependence of the injection process on laser pulse energy, shots containing electron beams with energy higher than 30 MeV (the lowest energy accepted in the single-shot magnetic spectrometer at full magnetic field strength) were studied. For the 190 μm diameter capillary, the threshold intensity was found to be $a_0 \simeq 0.75$ with 0.7 J energy laser and resulted in the generation of electron beams at 300 MeV containing a few pC of charge. For $a_0 \simeq 0.47$ with 0.9 J energy laser, generation of broad energy spectrum electron beams up to 400 MeV was observed. In case of the 225 μm capillary, the threshold intensity was found to be $a_0 \simeq 0.68$ and did not exhibit any dependence on laser energy from 0.9 J to 1.3 J. No beam generation occurred with lower energy laser beams. The 310 μm diameter capillary required high power operation (> 1.3 J/pulse) to generate any energetic electron beam. The injection threshold intensity was found to be $a_0 \simeq 1.4$, which corresponds to 35 TW laser power for a pulse duration of 38 fs. The threshold intensities should be regarded as tentative since experiments were not performed with identical parameters (density and delay)

for different capillaries. Nevertheless, a comparison of the threshold intensities from available data suggests that the threshold laser intensity is lower for smaller capillaries. The electron beam divergence was also found to depend on capillary diameter. Larger divergence beams were observed from the smaller diameter capillary. From those observations, a possible scenario may be either or both of the following: (a) the fact that the plasma channel has a smaller matched spot for smaller diameter[30] influences on the propagation of the laser pulse, which affects injection, and (b) transverse wakefields play a key role in self injection and e-beam properties in the capillary-guided LWFA (narrower channels result in larger transverse density gradients and larger transverse wakefields).

The performance of the accelerator was also found to be sensitive to the timing between discharge current and laser beam, consistent with the observed dependence of the guiding properties on the laser-discharge timing discussed above. Shown in Fig. 4 is the probability of observing electron beams above 30 MeV as a function of the delay. Here 100% injection means that the beam was always observed with those parameters. For the 190 μm diameter capillary, the timing was scanned from 25 to 140 ns with a density of $\simeq 3.0 \times 10^{18}$ cm^{-3} and $\simeq$ 0.9 J – 45 fs laser beam. The injection probability clearly follows the discharge current profile. Note that the probability also depends on the laser parameters and plasma density. It can be tuned to achieve 100% injection. For the 225 μm diameter capillary, the timing was scanned from 45 to 270 ns with a density of $\simeq 3.0 \times 10^{18}$ cm^{-3} and $\simeq$ 1.5 J, $\simeq$40 fs laser. At the beginning of the discharge current profile, 100% injection was obtained and injection terminated with the end of the discharge. Unlike the 190 μm diameter capillary, it did not follow the ripples on the current, but still showed some temporal structure. The 310 μm diameter capillary case with a density of $\simeq 4.1 \times 10^{18}$ cm^{-3} and $\simeq$ 1.7 J in a $\simeq$40 fs duration laser pulse is shown as well. Though it is not as clear as the 190 μm diameter capillary case, the injection probability for the 310 μm capillary weakly follows the temporal structure of the discharge current, having the maximum probability on top of the second ripple and less injection at the local minimums of the current profiles. Those features are consistent with the timing structure in the low power guiding performance shown in Fig. 3, where the guiding performance was shown to follow the discharge-current ripples as well.

The dependence of the probability of injection on plasma density was experimentally studied by changing the backing pressure of the hydrogen feed line. For the 190 μm diameter capillary, the plasma density was scanned from 2.7 to 3.8×10^{18} cm^{-3} with a 0.7 J, $\simeq$43

fs laser. The injection probabilities, averaged over delays between 60 ns and 100 ns, were $\simeq$70% and did not show significant dependence on the plasma density. For the 225 μm diameter capillary, the plasma density was scanned from 3.0 to 3.8×10^{18} cm^{-3} with a 1.1 J, $\simeq$41 fs laser. The injection probability, averaged over delays between 100 and 200 ns, was $\simeq$50% with a density of 3.0×10^{18} cm^{-3} and linearly increased to $\simeq$80% with a density of 3.8×10^{18} cm^{-3}. For the 310 μm diameter capillary, the plasma density was scanned from 4.1 to 4.9×10^{18} cm^{-3} with a 1.5 J, $\simeq$40 fs laser. The injection probability, averaged over delays between 100 and 250 ns, was $\simeq$5% with a density of 4.1×10^{18} cm^{-3} and linearly increased to $\simeq$80% with a density of 4.9×10^{18} cm^{-3}. Note that no electron beams were observed for densities below 4.1×10^{18} cm^{-3}. The probability of injection showed strong dependence on the plasma density and suggests that self modulation of the laser pulse may be responsible for the injection. Through the analysis, the timing dependence were averaged to extract density dependence. Note that by tuning the timing and the density, 100% injection can be performed with all capillaries for the above laser parameters.

The reproducible generation of a 0.5 GeV beam with 225 μm diameter capillary was reported previously[25]. With $\simeq$12 TW laser power, every laser shot resulted in an e-beam at 0.48 GeV $\pm$6% and an rms spread $\simeq$ 5%. A typical single-shot e-beam spectrum in the stable 0.5 GeV regime is shown in Fig. 5. As stated above, from the energy integrated vertical profile which is shown in Fig. 5 (c), the beam divergence was calculated and used to de-convolve the finite beam effect from space-integrated energy spread, which is shown in Fig. 5 (b). The energy spread of the beam in Fig. 5 is 5.6% rms. The electron beam parameters, namely beam energy and its spread and beam total charge were found to be sensitive to the discharge - laser timing and laser energy (power). Shown in Fig. 6 are the beam peak energy and total charge versus the timing and the normalized vector potential a_0. Also shown in Fig. 6 is the image of a typical electron beam out of the stable parameter regime. The laser pulse duration was kept at 70$\sim$80 fs, and the difference of the intensity comes from varying the laser energy, which was 0.9 J with $\pm$10% fluctuation. From the timing dependence, one can see that the beam energy was high and beam charge was low at $\simeq$ 150 ns. When the timing was not in the proper regime, the resultant electron beams had broad energy spread and contained higher charge than the mono-energetic beams, as shown in Fig.6 (c) where relatively large energy spread $\simeq$400 pC beams were observed for a delay of $\sim$160 ns and $a_0 = 0.85$. The laser beam intensity dependence shows that $\simeq$ 0.5

GeV electron beams containing 10's of pC were generated with laser power below $a_0 \simeq 0.78$. Above that laser intensity, electron beam energy starts to decrease while total charge of the beam increases, consistent with the higher amount of charge resulting in beam loading[13,32].

Electron beams with energies of 1 GeV were obtained in a 310 μm diameter channel capillary for $P = 40$ TW and a density of 4.3×10^{18} cm^{-3}. The single shot e-beam spectrum with the space-integrated energy profile and energy- integrated spacial profile is shown in Fig. 7. Using the previously stated method, the energy spread was found to be 2.5% (2.4% resolution) rms. Note that the measurement was resolution limited and as such the energy spread might have been smaller. A spatially displaced second beam is visible at $\simeq$0.8 GeV. Various mechanism such as hosing[33], beam loading[13,32], or dephasing may be responsible for the generation of the second beam. Multi-bunch features of this type were also observed in experiments with the other capillaries, and in numerical simulations owing to trapping of a second electron bunch in a wake bucket behind the first[13,32]. Electron beams were not observed for lower laser power (<38 TW) nor lower plasma density ($\leq 4.0 \times 10^{18}$ cm^{-3}). The operation of this larger diameter capillary was not as stable as the others (190 μm and 225 μm capillaries), probably due to (a) a greater difference between the spot size of the input laser beam and the matched spot size of the plasma channel, (b) weaker transverse variation of the plasma density leading to a reduction in transverse wavebreaking, and (c) the significance of small variations in the laser plasma parameters for this high power regime[13].

The generation of 1.0 GeV electron beam from 310 μm diameter capillary demonstrates the possibility of a compact GeV accelerator based on a few J/pulse class Ti:Sapphire laser system. The problem of stability may be overcome by a complete exploration of the parameter regime or controlled particle injection via laser triggering[34–37] or density ramp control[38].

From simple scaling laws one can estimate (assuming $a_0 \sim 1$) the energy gain as $W \sim E_0 L_{\rm deph} \sim (mc\omega_p/e)(\lambda_p^3/\lambda) \approx 1$ GeV and linear dephasing length as $L_{\rm deph} \approx 1$ cm for $n_p = 4 \times 10^{18}$ cm^{-3}. Although this simple dimensional analysis yields the correct order of magnitude estimates for the accelerator length and energy gain, a more accurate estimation of the energy gain would require the full plasma channel properties, the effects of laser pulse evolution, instabilities, self-focusing, and e-beam loading on the plasma wake. For example, simulations indicate that pulse evolution is essential to the trapping and acceleration process. As the pulse propagates, it self-modulates and steepens such that the plasma electrons are

completely blown out from the region of the axis (cavitation or bubble regime[39]), at which point electrons are self-trapped and accelerated from the background plasma, in a manner similar to that described in previous experiments on high quality beam production at the 100 MeV level[11,13].

IV. SUMMARY AND CONCLUSIONS

We have demonstrated the production of high quality electron beams up to 1 GeV from a centimeter-scale accelerator. This is the highest beam energy yet reported for a laser-driven accelerator, and the shortest accelerator of any type to accelerate electrons from rest to GeV energies. This was enabled by gas-filled capillary discharge waveguides that channeled relativistically-intense laser pulses over several centimeters of sufficiently low density plasma.

The performance of the capillary discharge channel guided accelerator was found to depend on capillary diameter, plasma density, laser-discharge timing, and laser pulse energy and peak power. Regimes in parameter space were found where reproducible self-trapped electron beams were generated with energy around 0.5 GeV.

The short wavelength of the plasma accelerating structure results in femtosecond duration bunches ($>$ 10 kA peak current), that are well suited for driving pulsed radiation sources. This offers the prospect of novel, compact, and intrinsically-synchronized sources of femtosecond electron pulses and radiation tunable from x-ray[40–42] to THz frequencies[43–45], as needed for pump-probe measurements in the basic and applied sciences. The GeV beams pave the way for compact femtosecond free electron lasers producing keV x-rays using existing cm-scale period undulators, which was not possible with 100 MeV-class beams. Furthermore, it is anticipated that longer accelerating structures can be made by staging capillary discharge waveguides[36], thereby opening a path of compact accelerators beyond the multi-GeV level for applications in high energy physics.

Acknowledgments

Work supported by the U.S. Department of Energy under contract DE-AC02-05CH11231 and the Engineering and Physical Sciences Research Council, UK. We greatly appreciate contributions from Catalin Filip, Estelle Michel, Brad Shadwick, Michael Dickinson, Don

Syversrud, Joe Wallig, Nathan Ybarrolaza, Weishi Wan, Mark Witney, Tom Rowlands-Rees and Dino Jaroszynski.

* Paper UI2 2, Bull. Am. Phys. Soc. **51**, 259 (2006).

† Also at Nuclear Professional School, University of Tokyo, Japan

‡ Presently at Oxford University, UK.

§ WPLeemans@lbl.gov; Invited speaker.

¶ Presently at Lawrence Berkeley National Laboratory, Berkeley, CA 94720

[1] A. Modena, Z. Najmudin, A. E. Dangor, C. E. Clayton, K. A. Marsh, C. Joshi, V. Malka, C. B. Darrow, C. Danson, D. Neely, and F. N. Walsh, Nature **377**, 606 (1995).

[2] D. Umstadter, S.-Y. Chen, A. Maksimchuk, G. Mourou, and R. Wagner, Science **273**, 472 (1996).

[3] A. Ting, C. I. Moore, K. Krushelnick, C. Manka, E. Esarey, P. Sprangle, R. Hubbard, H. R. Burris, and M. Baine, Phys. Plasmas **4**, 1889 (1997).

[4] C. Gahn, G. D. Tsakiris, A. Pukhov, J. Meyer-ter-Vehn, G. Pretzler, P. Thirolf, D. Habs, and K. J. Witte, Phys. Rev. Lett. **83**, 4772 (1999).

[5] W. P. Leemans, P. Catravas, E. Esarey, C. G. R. Geddes, C. Toth, R. Trines, C. B. Schroeder, B. A. Shadwick, J. van Tilborg, and J. Faure, Phys. Rev. Lett. **89**, 4802 (2002).

[6] V. Malka, S. Fritzler, E. Lefebvre, M. M. Aleonard, F. Burgy, J. P. Chambaret, J. F. Chemin, K. Krushelnick, G. Malka, S. P. D. Mangles, Z. Najmudin, M. Pittman, J. P. Rousseau, J. N. Scheurer, B. Walton, and A. E. Dangor, Science **298**, 1596 (2002).

[7] T. Hosokai, K. Kinoshita, A. Zhidkov, K. Nakamura, T. Watanabe, T. Ueda, H. Kotaki, M. Kando, K. Nakajima, and M. Uesaka, Phys. Rev. E **67**, 036407 (2003).

[8] T. Tajima and J. M. Dawson, Phys. Rev. Lett. **43**, 267 (1979).

[9] P. Sprangle, E. Esarey, A. Ting, and G. Joyce, Appl. Phys. Lett. **53**, 2146 (1988).

[10] S. Mangles, C. Murphy, Z. Najmudin, A. Thomas, J. Collier, A. Dangor, E. Divali, P. Foster, J. Gallacher, C. Hooker, D. Jaroszynski, A. Langley, W. Mori, P. Norreys, F. Tsung, R. Viskup, B. Walton, and K. Krushelnick, Nature **431**, 535 (2004).

[11] C. G. R. Geddes, C. Tóth, J. van Tilborg, E. Esarey, C. B. Schroeder, D. Bruhwiler, C. Nieter, J. Cary, and W. P. Leemans, Nature **431**, 538 (2004).

[12] J. Faure, Y. Glinec, A. Pukhov, S. Kiselev, S. Gordienko, E. Lefebvre, J.-P. Rousseau, F. Burgy, and V. Malka, Nature **431**, 541 (2004).

[13] C. G. R. Geddes, C. Tóth, J. van Tilborg, E. Esarey, C. B. Schroeder, D. Bruhwiler, C. Nieter, J. Cary, and W. P. Leemans, Phys. Plasmas **12**, 056709 (2005).

[14] C. G. R. Geddes, C. Toth, J. van Tilborg, E. Esarey, C. B. Schroeder, J. Cary, and W. P. Leemans, Phys. Rev. Lett. **95**, 145002 (2005).

[15] W. P. Leemans, C. W. Siders, E. Esarey, N. E. Andreev, G. Shvets, and W. B. Mori, IEEE Trans. Plasma Sci. **24**, 331 (1996).

[16] C. G. Durfee III and H. M. Milchberg, Phys. Rev. Lett. **71**, 2409 (1993).

[17] P. Volfbeyn, E. Esarey, and W. P. Leemans, Phys. Plasmas **6**, 2269 (1999).

[18] D. Kaganovich, A. Ting, C. I. Moore, A. Zigler, H. R. Burris, Y. Ehrlich, R. F. Hubbard, and P. Sprangle, Phys. Rev. E **59**, R4769 (1999).

[19] T. Hosokai, M. Kando, H. Dewa, H. Kotaki, S. Kondo, K. Nakajima, and K. Horioka, Opt. Lett. **25**, 10 (2000).

[20] D. J. Spence and S. M. Hooker, Phys. Rev. E **63**, 015401(R) (2001).

[21] M. C. Downer, C. Chiu, M. Fomyts'kyi, E. W. Gaul, F. Grigsby, N. H. Matlis, B. Shim, P. J. Smith, and R. Zgadzaj, *Advanced Accelerator Concepts. Eleventh Workshop*, AIP Conf. Proc. **647**, (American Institute of Physics, Woodbury, NY, 2002), p. 654.

[22] N. C. Lopes, G. Figueira, L. O. Silva, J. M. Dias, R. Fonseca, L. Cardoso, C. Russo, C. Carias, G. Mendes, J. Vieira, and J. T. Mendonça, Phys. Rev. E **68**, 035402 (2003).

[23] Y.-F. Xiao, H.-H. Chu, H.-E. Tsai, C.-H. Lee, J.-Y. Lin, J. Wang, and S.-Y. Chen, Phys. Plasmas **11**, L21 (2004).

[24] A. Butler, D. J. Spence, and S. M. Hooker, Phys. Rev. Lett. **89**, 185003 (2002).

[25] W. P. Leemans, B. Nagler, A. J. Gonsalves, C. Tóth, K. Nakamura, C. G. R. Geddes, E. Esarey, C. B. Schroeder, and S. M. Hooker, Nature Physics **2**, 696 (2006).

[26] W. P. Leemans, D. Rodgers, P. Catravas, C. G. R. Geddes, G. Fubiani, E. Esarey, B. Shadwick, R. Donahue, and A. Smith, Phys. Plasmas **8**, 2510 (2001).

[27] N. A. Bobrova, A. A. Esaulov, J. Sakai, P. V. Sasorov, D. J. Spence, A. Butler, S. M. Hooker, and S. V. Bulanov, Phys. Rev. E **65**, 016407 (2002).

[28] B. H. P. Broks, K. Garloff, and J. J. A. M. van der Mullen, Phys. Rev. E **71**, 016401 (2005).

[29] K. Makino and M. Berz, Nucl. Instrum. Methods Phys. Res. A **427**, 338 (1999).

[30] A. J. Gonsalves, T. P. Rowlands-Rees, B. H. P. Broks, J. J. A. M. van der Mullen, and S. M. Hooker, Phys. Rev. Lett. **98**, 025002 (2007).

[31] P. Sprangle, E. Esarey, and A. Ting, Phys. Rev. Lett. **64**, 2011 (1990).

[32] F. S. Tsung, R. Narang, W. B. Mori, C. Joshi, R. A. Fonseca, and L. O. Silva, Phys. Rev. Lett. **93**, 185002 (2004).

[33] S. Deng, C. D. Barnes, C. E. Clayton, C. O'Connell, F. J. Decker, R. A. Fonseca, C. Huang, M. J. Hogan, R. Iverson, D. K. Johnson, C. Joshi, T. Katsouleas, P. Krejcik, W. Lu, W. B. Mori, P. Muggli, E. Oz, F. Tsung, D. Walz, and M. Zhou, Phys. Rev. Lett. **96**, 045001 (2006).

[34] D. Umstadter, J. K. Kim, and E. Dodd, Phys. Rev. Lett. **76**, 2073 (1996).

[35] E. Esarey, R. F. Hubbard, W. P. Leemans, A. Ting, and P. Sprangle, Phys. Rev. Lett. **79**, 2682 (1997).

[36] D. Kaganovich, A. Ting, D. Gordon, R. F. Hubbard, T. Jones, A. Zigler, and P. Sprangle, Phys. Plasmas **12**, 100702 (2005).

[37] J. Faure, C. Rechatin, A. Norlin, A. Lifschitz, Y. Glinec, and V. Malka, Nature **444**, 737 (2006).

[38] S. Bulanov, N. Naumova, F. Pegoraro, and J. Sakai, Phys. Rev. E **58**, R5257 (1998).

[39] A. Pukhov and J. Meyer-ter-Vehn, Appl. Phys. B **74**, 355 (2002).

[40] P. Catravas, E. Esarey, and W. P. Leemans, Meas. Sci. Technol. **12**, 1828 (2001).

[41] E. Esarey, B. Shadwick, P. Catravas, and W. P. Leemans, Phys. Rev. E **65**, 056505 (2002).

[42] A. Rousse, K. T. Phuoc, R. Shah, A. Pukhov, E. Lefebvre, V. Malka, S. Kiselev, F. Burgy, J.-P. Rousseau, D. Umstadter, and D. Hulin, Phys. Rev. Lett. **93**, 135005 (2004).

[43] W. P. Leemans, C. G. R. Geddes, J. Faure, C. Tóth, J. van Tilborg, C. B. Schroeder, E. Esarey, G. Fubiani, D. Auerbach, B. Marcelis, M. A. Carnahan, R. A. Kaindl, J. Byrd, and M. Martin, Phys. Rev. Lett. **91**, 074802 (2003).

[44] W. P. Leemans, E. Esarey, J. van Tilborg, P. A. Michel, C. B. Schroeder, C. Tóth, C. G. R. Geddes, and B. A. Shadwick, IEEE Trans. Plasma Sci. **33**, 8 (2005).

[45] J. van Tilborg, C. B. Schroeder, C. V. Filip, C. Tóth, C. G. R. Geddes, G. Fubiani, R. Huber, R. A. Kaindl, E. Esarey, and W. P. Leemans, Phys. Rev. Lett. **96**, 014801 (2006).

FIG. 1: (Color) Schematic diagram of the capillary-guided laser wakefield accelerator. The plasma channel was formed in a hydrogen-filled capillary discharge waveguide (see inset). Hydrogen gas was introduced into the capillary waveguide using two gas slots in the 190 μm and 225 μm diameter capillary and three in the 310 μm capillary. A discharge was struck between two electrodes located at each end of the waveguide, using a high voltage pulsed power supply that utilized a 2.7 nF capacitor charged to 20 kV. The laser beam was focused onto the entrance of the capillary using an f/25 off-axis parabola (OAP). The guiding efficiency was measured using a pair of optical diodes (Diode 1 and 2) that monitored the amount of laser energy at the entrance and exit of the capillary. The laser beam exiting the capillary was monitored on a 12 bit CCD camera (20 μm resolution), after having been attenuated with a pair of reflective wedges and optical attenuators (not shown). The e-beam was analyzed using an integrating current transformer (ICT) and a 1.2 T broad-band magnetic spectrometer (energy range of 0.03–0.15 and 0.175–1.1 GeV in a single shot). The e-beam was deflected downward and detected using phosphor screens imaged onto four synchronously triggered CCD cameras (not shown).

FIG. 2: Calculated electron energy against the position on the phosphor screen with designed orbit (0 degree) and incident angle of ± 0.25 and ± 0.5 degree to the system. Based on the measured average angular fluctuation of 0.21 degree (rms), error bars for the experiments are also shown. (a) 1 GeV (+0.058, -0.052), and (b) 0.5 GeV (+0.026, -0.024).

FIG. 3: (Color) Capillary transmission at 5 TW peak input power versus time of arrival of the laser pulse after the onset of the discharge, and mode profiles of the input and output laser beam at 40 TW peak power. The averaged discharge current (red solid line, right axis) and laser pulse energy transmission (green dots, left axis) vs. arrival time of the laser at the capillary for laser pulses <5 TW are shown in (a). The blue dotted curve is the average transmission. The transverse spatial profiles of laser pulses with an input peak power of 40 TW at the entrance and exit of the 3.3 cm long gas-filled capillary discharge waveguide (190 μm diameter) are shown in (b) and (c), respectively. The blue (red) curve is the horizontal (vertical) lineout. The horizontal and vertical spot sizes at the entrance were $r_{sx} = 25$ μm and $r_{sy} = 27$ μm, respectively, and $r_{sx} = 31$ μm and $r_{sy} = 34$ μm at the exit. The plasma density was $\simeq 2.7 \times 10^{18}$ cm^{-3}. The 20% increase in spot size at the exit may be caused by imperfect mode matching or self focusing. The energy transmission at this laser power was about 65%. Combined with the increase in laser spot size this results in a decrease in laser peak fluence from 1.3×10^5 J/cm^2 to 0.5×10^5 J/cm^2. Assuming that the laser pulse duration remains constant between entrance and exit of the capillary, the peak intensity of the laser was reduced from 3 to 1.2 $\times 10^{18}$ W/cm^2.

FIG. 4: Probability of the observation of above 30 MeV electron beam (left) as a function of the delay between the onset of the current pulse and the arrival of the laser pulse (Solid line, right). Triangles: 190 μm diameter capillary scanned with a density of $\simeq 3.0 \times 10^{18}$ cm^{-3} for $\simeq$0.9 J, $\simeq$45 fs laser. Squares: 225 μm diameter capillary scanned with a density of $\simeq 3.0 \times 10^{18}$ cm^{-3} and $\simeq$ 1.5 J, $\simeq$40 fs laser. Circles: 310 μm diameter capillary with a density of $\simeq 4.1 \times 10^{18}$ cm^{-3} and $\simeq$ 1.7 J, $\simeq$40 fs laser beam. Note that the densities here are estimated axial electron densities.

FIG. 5: (Color) Typical single-shot e-beam spectrum from the stable 0.5 GeV regime of 225μm diameter capillary-guided accelerator with a density of $\simeq 3.5 \times 10^{18}$ cm^{-3} and input laser power of 12 TW. (a) Image of the electron beam in pC/GeV/steradian (SR), with the energy in horizontal axis and the non-deflected plane in vertical axis. (b) The space-integrated spectrum of the beam in pC/GeV. (c) Energy-integrated spatial profile of the beam in pC/mrad. The total charge was $\simeq$50 pC, and the beam divergence was 2.0 mrad (rms). Under the assumption of a symmetric beam profile, the energy spread of the beam was estimated to be 5.6% (rms) with resolution of 1.1% (rms). The horizontal error bar in (b) (+0.056, -0.055) comes from the convolution of the uncertainty in the energy (+0.026, -0.024, see Fig. 2) and the actual fluctuation from measurement ($\pm$0.05) of $0.50^{+0.026}_{-0.024}$ GeV. The vertical error bar in (b) is the convolution of the uncertainty in calibration of the phosphor screen as a charge monitor ($\pm$17%) and the actual shot-to-shot fluctuation in charge ($\pm$ 30%), therefore, $\pm$ 34%.

FIG. 6: (Color) Peak beam energy and total charge versus the laser-discharge timing (a) and the normalized vector potential (b), and a typical electron beam spectrum outside of the proper parameter regime for stable 0.5 GeV generation (c). The e-beam in (c) contained $\simeq$400 pC of charge, the laser-discharge timing was 162 ns, and $a_0 = 0.85$.

FIG. 7: (Color) Single-shot e-beam spectrum from a 310μm diameter capillary-guided accelerator with a density of 4.3×10^{18} cm^{-3} and input laser power of 40 TW. (a) Image of the electron beam in pC/GeV/SR, with the energy in horizontal axis and the non-deflected plane in vertical axis. (b) The space-integrated spectrum of the beam in pC/GeV. (c) Energy-integrated spacial profile of the beam in pC/mrad. The total charge was $\simeq$30 pC, and the beam divergence was 1.6 mrad (rms). Under the assumption of a symmetric beam profile, the energy spread of the beam was estimated to be 2.5% (rms) with resolution of 2.4% (rms). The horizontal error bar in (b) comes from the uncertainty in the energy (+0.058, -0.052, see Fig. 2). The vertical error bar in (b) is due to the uncertainty in calibration of the phosphor screen as a charge monitor ($\pm$17%). A second beam at 0.8 GeV is also visible in (a).

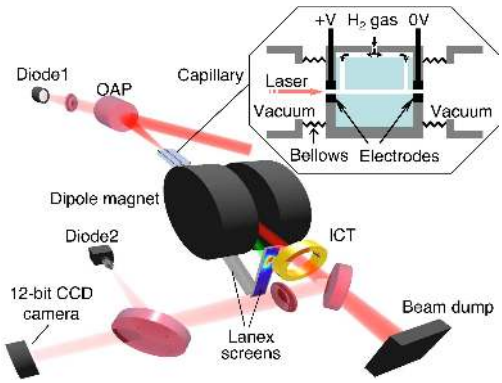
+V
H_2 gas
0V
Diode1
OAP
Capillary
Laser
Vacuum
Vacuum
Bellows
Electrodes
Dipole magnet
Diode2
ICT
12-bit CCD
camera
Beam dump
Lanex
screens

Fig.1

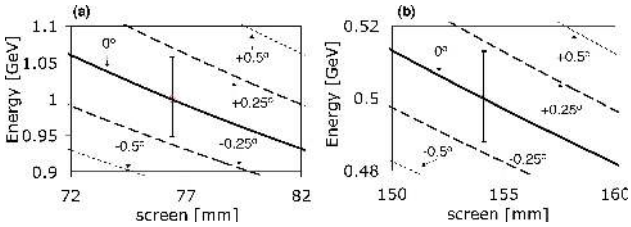
(a)
(b)
Energy [GeV]
screen [mm]
0°
+0.5°
+0.25°
-0.5°
-0.25°
1.1
1.05
1
0.95
0.9
72
77
82
0.52
0.5
0.48
150
155
160

Fig.2

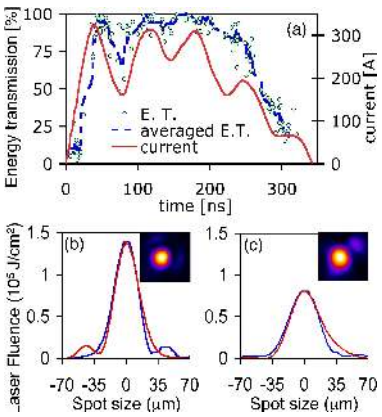
Energy transmission [%]
100
75
50
25
0
(a)
300
200
100
0
current [A]
E. T.
averaged E.T.
current
0
100
200
300
time [ns]
Laser Fluence (10^5 J/cm^2)
1.5
1
0.5
0
(b)
(c)
-70 -35 0 35 70
Spot size (μm)
-70 -35 0 35 70
Spot size (μm)

Fig.3

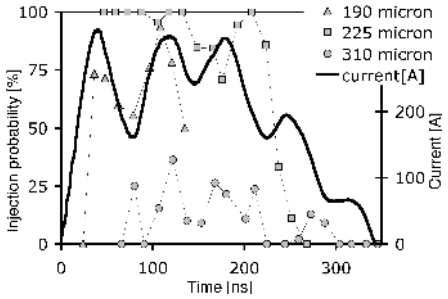
100
75
50
25
0
Injection probability [%]
0
100
200
300
Time [ns]
200
100
0
Current [A]
190 micron
225 micron
310 micron
current[A]

Fig.4

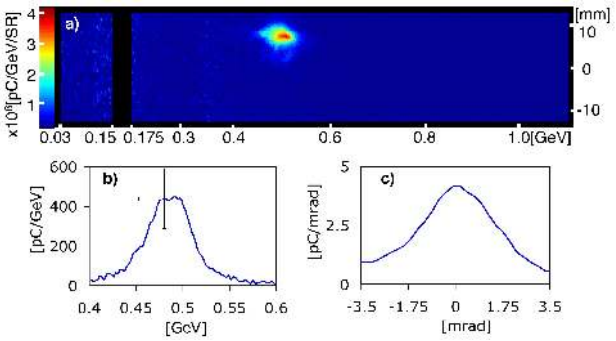
a)
x10⁶[pC/GeV/SR]
4
3
2
1
[mm]
10
0
-10
0.03 0.15 0.175 0.3 0.4 0.6 0.8 1.0[GeV]
b)
[pC/GeV]
600
400
200
0
0.4 0.45 0.5 0.55 0.6
[GcV]
c)
[pC/mrad]
5
2.5
0
-3.5 -1.75 0 1.75 3.5
[mrad]

Fig.5

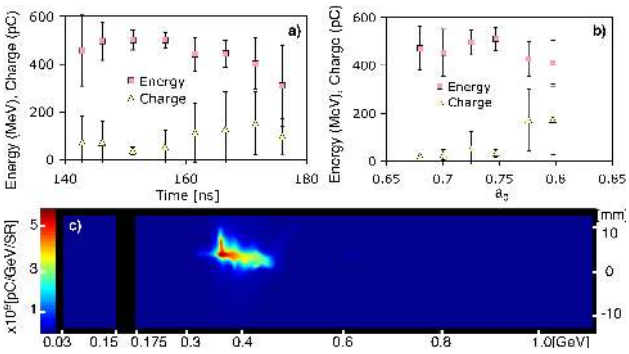
a)
b)
c)
Energy (MeV), Charge (pC)
Energy (MeV), Charge (pC)
Energy
Charge
Time [ns]
a_0
x10^6[pC/GeV/SR]
[mm]
0.03
0.15
0.175
0.3
0.4
0.6
0.8
1.0[GeV]

Fig.6

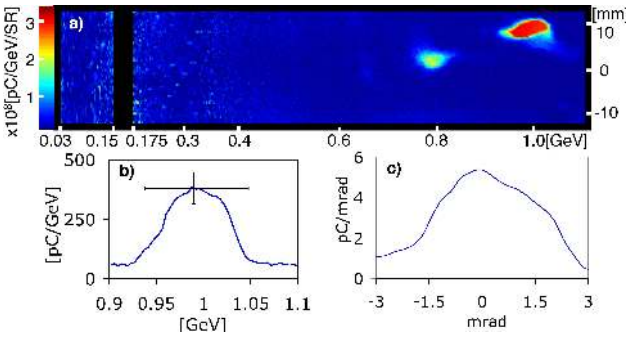
x10⁹[pC/GeV/SR]
3
2
1
a)
[mm
10
0
-10
0.03 0.15 0.175 0.3 0.4 0.6 0.8 1.0[GeV]
500
250
0
[pC/GeV]
b)
0.9 0.95 1 1.05 1.1
[GeV]
6
4
2
0
pC/mrad
c)
-3 -1.5 0 1.5 3
mrad

Fig.7